ENVIRONMENTAL RESEARCH
COMMUNICATIONS

PAPER • OPEN ACCESS

Heterogeneous warming impacts of desert wind farms on land surface temperature and their potential drivers in Northern China

To cite this article: Naijing Liu *et al* 2022 *Environ. Res. Commun.* **4** 105006

Environmental Research Communications

PAPER

Heterogeneous warming impacts of desert wind farms on land surface temperature and their potential drivers in Northern China

Naijing Liu[1,2], **Xiang Zhao**[1,2,*], **Xin Zhang**[3], **Jiacheng Zhao**[1,2], **Haoyu Wang**[4] and **Donghai Wu**[5]

[1] State Key Laboratory of Remote Sensing Science, Jointly Sponsored by Beijing Normal University and Aerospace Information Research Institute of Chinese Academy of Sciences, Faculty of Geographical Science, Beijing Normal University, Beijing 100875, People's Republic of China
[2] Beijing Engineering Research Center for Global Land Remote Sensing Products, Institute of Remote Sensing Science and Engineering, Faculty of Geographical Science, Beijing Normal University, Beijing 100875, People's Republic of China
[3] School of Computing, Mathematics and Digital Technology, Manchester Metropolitan University, Manchester M1 5GD, United Kingdom
[4] School of Earth and Space Sciences, Peking University, Beijing 100871, People's Republic of China
[5] Department of Ecology and Evolutionary Biology, Cornell University, Ithaca, NY 14853, United States of America
* Author to whom any correspondence should be addressed.

E-mail: zhaoxiang@bnu.edu.cn

Keywords: wind farm, land surface temperature, desert, spatial heterogeneity, remote sensing

Supplementary material for this article is available online

OPEN ACCESS

RECEIVED
28 June 2022

REVISED
3 October 2022

ACCEPTED FOR PUBLICATION
18 October 2022

PUBLISHED
31 October 2022

Abstract

To address rapid climate change, wind energy has been widely developed in China in the last two decades. However, wind farm (WF) turbulence effects can change the local climate by redistributing temperature, humidity, and heat fluxes. Previous studies indicate that WFs can significantly increase nighttime land surface temperature (LST); however, their conclusions are mainly derived from individual WFs and ignore heterogeneous impacts among multi-WFs in China. Another large source of uncertainty is that the WFs used in previous studies are mainly located in croplands or grasslands, which may obscure direct WF impacts because of the interactions between vegetation and the atmosphere. In this study, we detect impacts with MODIS LST products during 2001–2018 at sixteen WFs in the desert of northern China. The results suggest that the averaged warming impacts of WFs on LST are similar between nighttime (0.237 °C) and daytime (0.250 °C). However, the uncertainty is much greater for daytime (SD = 0.519 °C) than for nighttime (SD = 0.146 °C) due to spatially heterogeneous impacts of desert WFs on LST. Optimal structural equation models suggest that wind speed, precipitation, and distribution patterns of wind turbines mainly explain the spatial heterogeneity of the desert WF impacts on nighttime LST. Given the rapid development of WFs globally, the local warming impacts of WFs and their corresponding mechanisms should be highlighted as a high priority in the fields of energy and climate.

1. Introduction

Wind energy plays a major role in renewable energy exploitation, which provides a massive amount of clean energy and reduces greenhouse gas emissions by fossil fuels (Veers *et al* 2019). The World Wind Energy Association reported that the sum of the global wind turbine capacity has been rapidly growing in the past two decades. It reached approximately 600 Gigawatts by the end of 2018, which could cover 6% of the total human electricity demand (World Wind Energy Association 2019). Moreover, there has been an exploding increase in wind turbine installation in China since the beginning of the 21st century, accounting for approximately one-third (210 Gigawatts) of the global wind energy by the end of 2018 (Chinese Wind Energy Association 2019).

In spite of the fact that the main purpose of rapid wind energy development is to reduce fossil fuel emissions and mitigate global warming, environmental side effects have also appeared as the number of wind turbines have largely expanded (Dai *et al* 2015, Tabassum *et al* 2014, Wang and Wang 2015). Wind turbines usually generate

wake turbulence by the rotating blades, which can redistribute the surrounding temperature, humidity, and heat fluxes (Roy and Traiteur 2010, Zhou *et al* 2012, Armstrong *et al* 2014). Therefore, the large-scale construction of wind farms (WFs) may change the local climate, which depends on the stability of the atmospheric boundary layer (ABL) (Armstrong *et al* 2014, Wu and Archer 2021). When the ABL is stable with cooler air near the ground and warmer air in the upper layer, which is more probable to happen in the nighttime, the rotations of wind turbine blades mix the warmer air layer and the air cooler near the surface and heat the land surface. However, when the ABL is unstable, with warmer air near the surface and cooler air in the upper layer, the WF impact on daytime LST is more complicated. Rotations of the wind turbine blades mix the cooler upper air and the warmer near-surface air and cool down the land surface (Miller and Keith 2018, Zhou *et al* 2020, Qin *et al* 2022), solar radiation heats the surface and creates upward convection. Besides, when the ABL is neutral, the temperatures of upper and lower air layers are approximate and the heat convection is near zero. The rotation has little impact on the surface. In addition to the ABL process, the conversion of the kinetic energy of the wind into the electric power of the wind turbines also produces massive heat (Corten 2000, Nematollahi *et al* 2019), which may also contribute to the warming effects.

Based on remote sensing time series, previous studies indicated that WFs can significantly increase nighttime land surface temperature (LST) (Zhou *et al* 2013 2012, Slawsky *et al* 2015, Tang *et al* 2017), however, the impacts on daytime LST are divergent (Zhou *et al* 2013 2012, Slawsky *et al* 2015, Tang *et al* 2017, Wu *et al* 2019). According to multiple model simulations at different scales, a WF can lead to a 0.2 °C–2.16 °C warming of local temperature (Keith *et al* 2004, Vautard *et al* 2014, Xia *et al* 2017, Li *et al* 2018, Pryor *et al* 2018), which suggests large climatic impacts of WFs.

Although there are some preliminary conclusions in terms of the WF impacts on LST, two main aspects should be further considered to obtain a clear picture of the driving processes. First, previous conclusions were mainly derived from individual WFs in China, which ignored background environmental effects. For example, the magnitude of the local wind speed may affect WF impacts by altering the speed of their wind blade rotation (Abo-Khalil *et al* 2019, Tahir *et al* 2019). The other uncertainty source is that the WFs used in previous works were mainly located in croplands and grasslands, which may obscure the direct WF impacts because of the interactions between vegetation and the atmosphere (Feng *et al* 2016, Grossiord *et al* 2020). For example, human irrigation in croplands can cool the air temperature by evapotranspiration (Payero *et al* 2008, Kurylyk *et al* 2014), which will weaken the WF impacts on LST observed by remote sensing. To minimize the effects of vegetation-atmosphere interactions, desert WFs with no vegetation cover are the optimal study areas for detecting the direct WF impacts on LST.

Considering the two main uncertainty sources, in this study, 16 desert WFs (with $\geqslant$ 100 wind turbines in each WF) were selected to evaluate the WF impacts on local LST in northern China. Based on a remote sensing time series, we analyzed the WF impact on the local daytime and nighttime LST by comparing the WF areas and their surrounding control areas (buffer). Then, the spatial distribution of the impact was evaluated at a grid scale in both the WFs and buffers. Furthermore, based on the structural equation model, we ultimately detected the possible environmental drivers of the spatial heterogeneity of desert WF impacts on daytime and nighttime LSTs.

2. Materials and methods

2.1. Study area

In this study, we extract 7077 wind turbines distributed in 16 desert wind farms (WFs) through the deep learning algorithm You Only Look Once (YOLO) (Zhang *et al* 2020) in 2018, which are the world's largest desert WF group. YOLO is a fast, high-efficient, and high-precision object detection approach based on a single neural network (Redmon *et al* 2016). The number of wind turbines installed at the WFs vary from 100 to 1965 (figure 1(a) and table S1). Shuttle Radar Topography Mission (SRTM) datasets (Jarvis *et al* 2008) are used to represent the elevation (figure S1). The mean annual Moderate Resolution Imaging Spectroradiometer (MODIS) normalized difference vegetation index (NDVI) of the 16 WFs is lower than 0.1 (table S1). Based on the SoilGrids datasets (Hengl *et al* 2017), there are 4 soil types among the 16 WFs, and 12 WFs are covered by gypsisols. The following analyses are based on 16 WFs, and further analyses have been made on 12 gypsisols WFs to restrict the potential thermal property differences brought by soil components.

To detect the WF impact, a comparison strategy is widely used between WF pixels and their surrounding control region (buffer) (Zhou *et al* 2012, Slawsky *et al* 2015, Tang *et al* 2017). The WF areas are extracted based on 1 km* 1 km pixels to ensure that every pixel contains at least one wind turbine. The buffer is built as 1 km* 1 km pixels 5 to 9 km outside the WF to avoid any air turbulence influence caused by wind turbines (figure 1(b)). The wake effect of wind turbines generates turbulence that spreads for kilometers downwind, the buffer should be outside the wake range. Meanwhile, the buffer should not be too far from the WF to share a similar climate

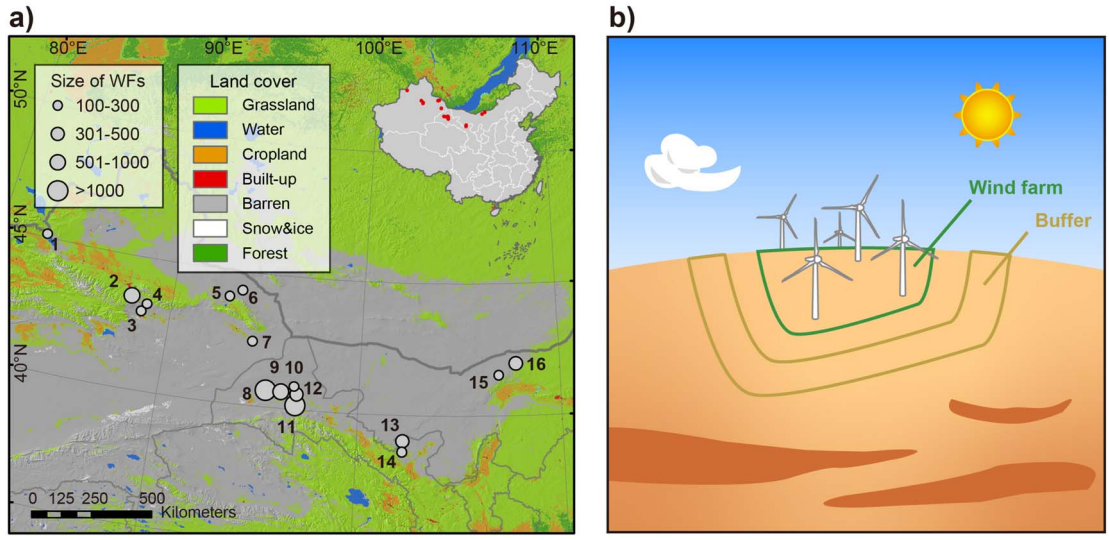

Figure 1. Distribution of the 16 WFs and the concept for the study area. (a) The spatial distribution of the 16 WFs, which are mainly located in the Takla Makan and Gobi deserts. The WF sizes are represented by symbols of different magnitudes, and the base map is the MODIS MCD12Q1 International Geosphere-Biosphere Programme (IGBP) land cover classification in 2018. (b) The concept for the wind farm pixels (WFPs) and buffer pixels (BUPs).

background (Zhou *et al* 2012, Tang *et al* 2017, Qin *et al* 2022). The desert pixels are finally filtered by MCD12Q1 IGBP land cover data (figure S2), the filtered pixels are defined as wind farm pixels (WFPs) and buffer pixels (BUPs) in the following text.

2.2. Datasets

2.2.1. Land surface temperature

To explore the spatial heterogeneity of WF impacts on desert LST, we use the Moderate Resolution Imaging Spectroradiometer (MODIS) MOD11A2 Land Surface Temperature (LST) time series between 2001 and 2018. The temporal resolution of MODIS LST is 8 days, and the spatial resolution is 1 km. Furthermore, MODIS provides both daytime (10:30 AM) and nighttime (10:30 PM) LST products (Wan, Hook, and Hulley 2015), which can help us better understand the WF impacts on the local climate. Further, we use MODIS Aqua LST time series of MYD11A2 as a supplementary test, the spatial and temporal resolutions are the same as MOD11A2, and the overpass time is 1:30 AM in the nighttime and 1:30 PM in the daytime.

2.2.2. Environmental factors

Four kinds of related environmental factors are used to explain the spatial heterogeneity of the WF impact on desert LST. First, the WorldClim precipitation and Tropical Rainfall Measuring Mission (TRMM) 3B43 monthly precipitation datasets are used. The WorldClim precipitation datasets are downscaled from the Climatic Research Unit (CRU), the spatial resolution is 2.5 arc minutes, and the temporal resolution is monthly (Fick and Hijmans 2017). The TRMM precipitation product algorithmically merges microwave data from multiple satellites. The spatial range is 50°S–50°N globally with a spatial resolution of 0.25° *0.25° (Kummerow *et al* 1998). Second, wind speed (50 m above ground) is derived from the Modern-Era Retrospective analysis for Research and Applications Version 2 (MERRA-2) monthly datasets (Gelaro *et al* 2017), with a spatial resolution of 0.625°*0.5°. The height of the wind speed is close to the blades of the wind turbines. Third, topography factors, including elevation and surface roughness, are used. The elevation is derived from the SRTM DEM dataset with a spatial resolution of 90 m (Jarvis *et al* 2008). Surface roughness is provided by the Sentinel-1 Synthetic Aperture Radar (SAR) Ground Range Detected (GRD) dataset, which is updated daily at a spatial resolution of 10 m and the preprocessing is already radiometric and terrain-corrected (Torres *et al* 2012). Fourth, soil properties, including soil type and sand content, are obtained from the SoilGrids datasets (Hengl *et al* 2017), which are modeled and fitted from more than 230000 soil profile observations at a spatial resolution of 250 m.

2.2.3. Wind farm shape factors

In addition to environmental drivers, WF shape factors are also used to explain the different WF impacts on the desert LST. The WF shape factors include the shape index, patch density, landscape division index, and mean

Euclidean nearest-neighbor distance, which can be calculated via the Fragstates platform (version 4.2.1) (McGarigal 1995). These factors describe the distribution of wind turbines within WF in different dimensions.

First, the shape index represents the ratio of the perimeter and area of patches in a WF, which can be calculated as:

$$SI_i = \frac{0.25 * p_i}{\sqrt{a_i}} \tag{1}$$

where SI_i is the shape index of the WF; i is the serial number of the WF; p_i is the perimeter of the WF (m); and a_i is the area of the WF (m^2). The shape index usually increases as the patches in a WF become more irregular and fragmented.

Second, the patch density indicates the number of patches within 100 hectares, which can be calculated as:

$$PD_i = \frac{N_i}{a_i} * 100 * 10000 \tag{2}$$

where PD_i is the patch density of the WF; i is the serial number of the WF; N_i is the number of patches in the WF; and a_i is the area of the WF (m^2). The patch density increases when there are more patches in a WF. A patch is an independent group of WFs pixels using the 8-neighbor rule in our study.

Third, the landscape division index is the divisive level of the WF, which can be calculated as:

$$LDI_i = 1 - \sum_{j=1}^{n}\left(\frac{a_{ij}}{a_i}\right)^2 \tag{3}$$

where LDI_i is the landscape division index of the WF; i is the serial number of the WF; n is the number of patches of WFs; a_{ij} is the area of patch j in the WF (m^2); and a_i is the total area of the WF (m^2). The landscape division index is closer to 1 when the WF is more fragmented.

Fourth, the mean Euclidean nearest-neighbor distance is calculated as:

$$MED_i = \frac{\sum_{j=1}^{n} h_{ij}}{n} \tag{4}$$

where MED_i is the mean Euclidean nearest-neighbor distance of the WF; i is the serial number of the WF; n is the number of patch pairs of WFs; and h_{ij} is the distance to the nearest neighboring patch (m). The mean Euclidean nearest-neighbor distance increases when the nearest patches within the WF get further.

2.2.4. Soil thermal admittance

To explore the relationship between surface thermal properties and WFs LST impacts, we calculate thermal admittance of 16 WFs as follows:

$$\mu = \sqrt{Ck} \tag{5}$$

where μ is thermal admittance by $J\,m^{-2}\,s^{-1/2}\,K^{-1}$, C is heat capacity by $J\,m^{-3}\,K^{-1}$, k is thermal conductivity by $J\,s^{-1}\,m^{-1}\,K^{-1}$ (Oke *et al* 1991, Runnalls and Oke 2000), heat capacity could be estimated by:

$$C = \sum f_{s_i} C_{s_i} + f_w C_w + f_a C_a \tag{6}$$

where f_x represent the volume fraction of solid, water, and gas components, and C_x are heat capacity of each component (Meyers 2002). The volume fractions of clay, silt, and sand are given by the SoilGrids dataset, while water volume fractions are provided by climate change initiative (CCI) soil moisture with daily temporal and 0.25° spatial resolution (Dorigo *et al* 2017, Gruber *et al* 2019). The volume fraction of air is set to 0.25 in this study. The heat capacity of clay, silt, sand, water, and air are 1.5, 1.5, 1.4, 4.2, and 0.0012 $MJ\,m^{-3}\,K^{-1}$ (Pahud 2002).

The thermal conductivity could be calculated as:

$$k = \frac{(k_{sat} - k_{dry})\kappa S_r}{1 + (\kappa - 1)S_r} + k_{dry} \tag{7}$$

where k_{sat} and k_{dry} are saturated and dry thermal conductivities of soil. S_r is the degree of saturation, which is set to 0.7 in our study. κ is the empirical fabric factor set to 3.55 (Côté and Konrad 2005). k_{sat} and k_{dry} could be calculated by:

$$k_{sat} = k_s{}^{f_s} k_w{}^{f_w} \tag{8}$$

$$k_{dry} = \chi \times 10^{-\eta n} \tag{9}$$

where k_s and k_w are thermal conductivities of solid and water components (Barry-Macaulay *et al* 2015). The thermal conductivities of clay, silt, sand, and water are 2.9, 2.9, 5.5, and 0.6 $J\,s^{-1}\,m^{-1}\,K^{-1}$. χ and η are empirical

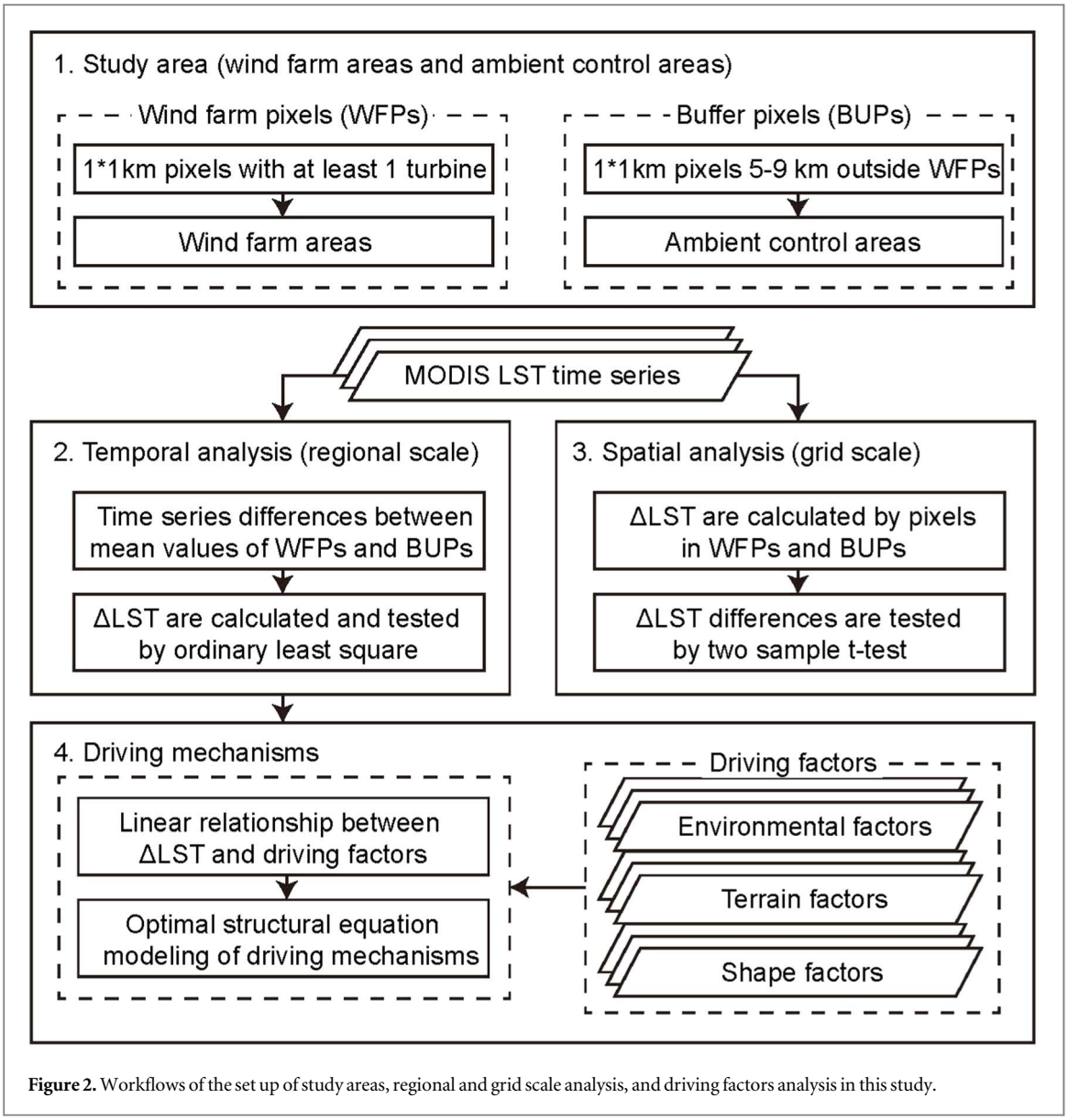

Figure 2. Workflows of the set up of study areas, regional and grid scale analysis, and driving factors analysis in this study.

soil type parameters that account for particle shape effect, which are set to 0.75 and 1.2. n is porosity and set to 0.43 in this study (Côté and Konrad 2005).

2.3. Methods

2.3.1. Wind farm impacts on land surface temperature

The spatial distribution of the WFPs and BUPs is close (~5 km distance) for each WF (figure 1(b)). Because they usually have similar regional background climate conditions, signals derived from the LST differences between WFPs and BUPs mainly represent the impacts of the WF (Zhou *et al* 2020). In this study, we used three different methods to determine the desert WF impacts on LST. The methods and the workflows of this study are given in figure 2.

The first method is the trend in the LST differences time series on regional scale, which can be expressed as:

$$\Delta LST_{i,j} = LST_{WFPs,i,j} - LST_{BUPs,i,j} \tag{10}$$

where $LST_{WFPs,i,j}$ is the mean annual LST in the WFPs in year j; i is the serial number of the WF; $LST_{BUPs,i,j}$ is the mean annual LST in the BUPs in year j; and $\Delta LST_{i,j}$ is the LST difference between the WFPs and BUPs. The time series of the $\Delta LST_{i,j}$ are constructed between 2001 and 2018 on the Google Earth Engine (Gorelick *et al* 2017). The trends in the $\Delta LST_{i,j}$ time-series are calculated via the slopes of ordinary least squares, and the significance of the trend is tested on at a level of 0.05. The impacts of WFs on LST (ΔLST) between 2001 and 2018 are the results of slopes multiplied by the period length of 18 years.

The second method is calculating the ordinary least square slopes and then the ΔLST between 2001 and 2018 at a grid scale. Then, we compare the pixel trends of LST between the WFPs and BUPs using a two-sample t-test

at a significance level of 0.05. If the ΔLST in the WFPs are significantly larger than those in BUPs, they could be considered significant warming impacts of WF.

The third method is to compare the preconstruction and postconstruction periods of the WFs at a grid scale. We define the postconstruction period as 2016–2018 and the preconstruction period as 2001–2003. Then, we compare the $_{\triangle}$LST between the WFPs and BUPs using a two-sample t-test at a significance level of 0.05.

2.3.2. Driving factor analyses with structural equation modeling

To determine the possible driving processes of the spatial heterogeneity of the desert WFs on LST, we first build linear relationships between the trends in the ΔLST (daytime and nighttime) and 15 environmental factors (i.e., climate, terrain, soil, and shape factors) among the 16 WFs. The coefficients of determination (R^2) are used to evaluate the robustness of the relationships. Then, based on *a priori* knowledge, we use structural equation modeling (SEM) to find the main driving factors of the spatial heterogeneity of the desert WFs on daytime and nighttime LST. The SEM is a multivariate statistical model used for complex relationships between directly and indirectly observed variables by multivariate statistical techniques of factor analysis and path analysis (Maruyama 1997). During the model optimization, the individual path coefficients with $p > 0.05$ are removed to obtain a minimum chi-square value (χ^2), Akaike information criterion (AIC), and maximum coefficient of determination (R^2). To eliminate the potential effects of soil properties, we also establish an SEM with the 12 WFs covered by gypsisols.

3. Results

3.1. Wind farm impacts on land surface temperature at a regional scale

Based on the MODIS LST time series from 2001 to 2018 in the 16 desert WFs, the results suggest that average ΔLST between the WFPs and BUPs is significantly increasing for both daytime and nighttime, which indicates that WFs increase the local temperature. The averaged warming impacts of WFs on LST are comparable between nighttime (0.237 °C) and daytime (0.250 °C) (figures 3(a), (d)); however, the uncertainty is much larger for daytime (SD = 0.519 °C) than for nighttime (SD = 0.146 °C). This suggests that the WF impacts on nighttime LST are more consistent than those on daytime LST.

For daytime LST (figure 3(b), figure S3), 10 of the 16 WFs show warming impacts, and 5 of those are significant ($p < 0.05$). The range of the WF warming impacts is between 0.368 °C at WF No. 3 and 1.456 °C at WF No. 13. However, 6 WFs suggest cooling impacts on LST, which range from −0.016 °C to −0.729 °C. In contrast, the WF impacts on nighttime LST are more robust (figure 3(e), figure S4). Specifically, 14 of the 16 WFs show warming impacts, and 10 WFs are significant ($p < 0.05$). The range of the WF warming impacts at nighttime is between 0.181 °C at WF No. 3 and 0.543 °C at WF No. 11. Only two WFs (No. 2 and No. 4) suggested nonsignificant cooling impacts on LST. Interestingly, the WFs with significant impacts on daytime and nighttime LST are mainly located at the center of our study area (WF No. 5-WF No. 11).

In addition to the WF impacts at an annual scale, we also analyzed the WF impacts on daytime and nighttime LST in different seasons (i.e., spring, summer, autumn, and winter). Similar to those at the annual scale, the WF impacts on daytime LST are more divergent than those on nighttime LST (figure S5). For daytime, the average ΔLST range from 0.063 °C in spring to 0.244 °C in winter. In contrast, for nighttime, the maximum impacts of the WFs are in summer (0.285 °C) and the minimum impacts of the WFs are in autumn (0.188 °C).

3.2. Wind farm impacts on land surface temperature at the grid scale

In addition to the regional scale, the ΔLST are also applied at the grid scale to detect the WF impacts on LST (see Methods). For daytime, LST in the WFPs rises 0.206 °C or 0.255 °C (23.28% or 25.71%) faster than the BUPs between preconstruction (2001–2003) and postconstruction (2016–2018) or 18 years (2001–2018) periods (figures S6(a)(c)). Among 16 WFs, the largest warming impacts occur at WF No. 13 with 1.434 °C warmer in WFPs than BUPs in 18 years period (figure 4(m)). In contrast, WF No. 7 shows the most obvious cooling effect of −0.749 °C (figure 4(g)).

For nighttime, the averaged ΔLST is 0.231 °C or 0.172 °C, which is 30.92% or 21.03% larger in the WFPs than in the BUPs between preconstruction and postconstruction or 18 years periods (figures S6(b) (d)). The largest warming impact occurs at WF No. 11, the LST in the WFPs gets warmer 0.555 °C faster than in the BUPs, while in WF No. 2, WFPs get cooler by −0.037 °C (figure 5). Furthermore, the differences between the preconstruction and postconstruction periods of the WFs at the grid scale also suggest similar patterns of the WF impacts on daytime and nighttime LST (figures S7, S8).

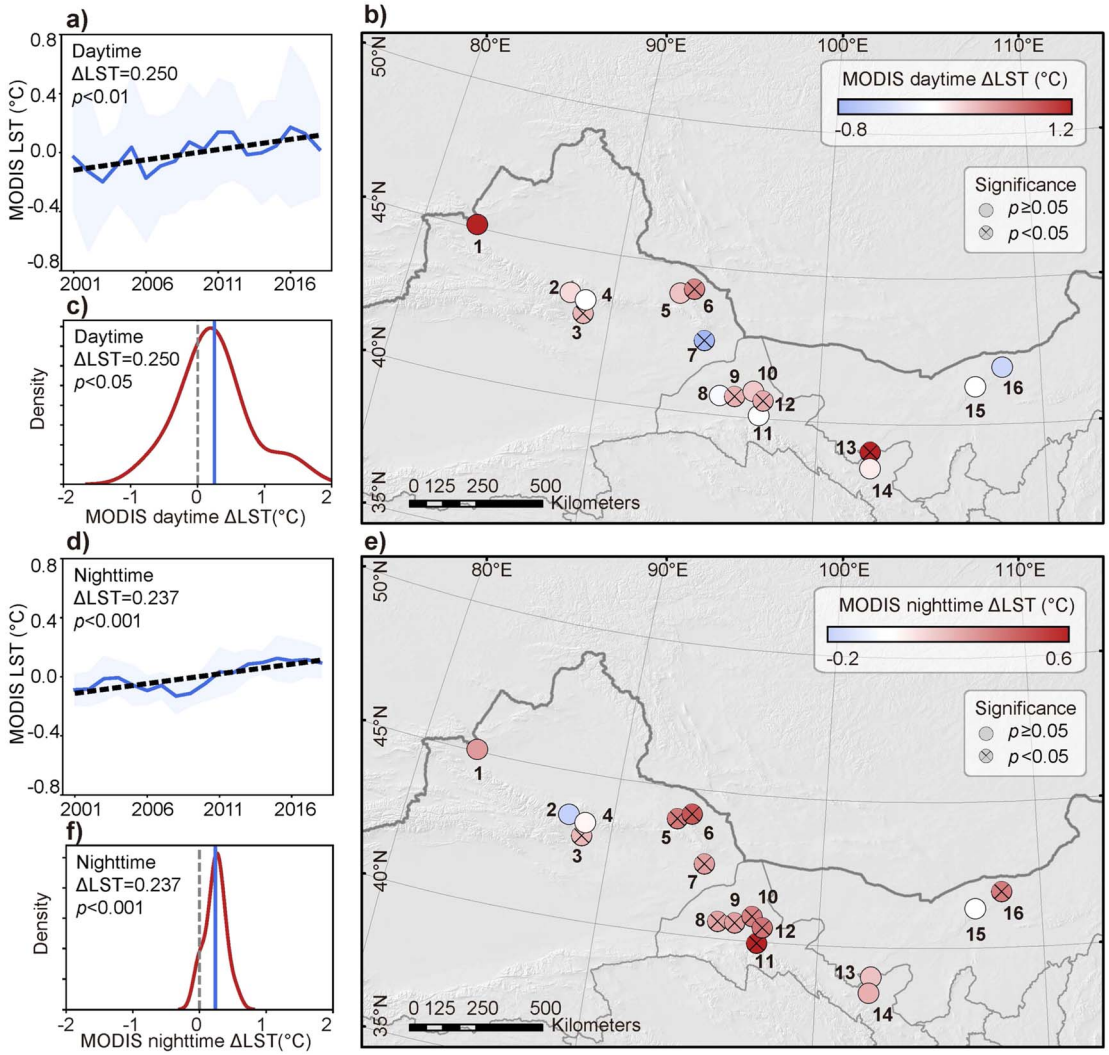

Figure 3. MODIS daytime and nighttime time-series ΔLST at 16 WFs from 2001 to 2018. (a), (d) averaged MODIS daytime and nighttime ΔLST time-series in 16 desert WFs. The ΔLST and significances of the ΔLST trends are given. The shaded ranges are the standard deviations of the average time series. (b), (e) the spatial distribution and significances of annual daytime and nighttime ΔLST at the 16 WFs. (c), (f) the distributions of the ΔLST values at the 16 WFs. The averaged ΔLST values and the significances of one-sample t-tests are given.

3.3. Driving factors of wind farm impacts on land surface temperature

To understand the potential mechanisms behind the different WF impacts on annual mean daytime and nighttime LST, linear regressions between the ΔLST and environmental factors are first established at the 16 WFs (figures S9, S10). For nighttime LST, the most robust relationship is found between the ΔLST and annual precipitation ($R^2 = 0.24$). For daytime, the highest R^2 is observed between the ΔLST and the Δ surface roughness ($R^2 = 0.21$). For other factors, the results suggest that the relationships with the ΔLST are weak. When we establish the relationships in the 12 WFs covered by gypsisols, the relationships become more robust, which indicates that soil types might also affect the spatial heterogeneity of the desert WF impacts on daytime and nighttime LST (figures S11, S12).

Based on *a priori* knowledge of WF affected LST, SEM is used to find the main driving factors for the spatial heterogeneity of desert WFs on daytime and nighttime LST. After model optimization based on χ^2, AIC, and maximum R^2, three factors, including the shape index, wind speed, and annual precipitation, explain 60% of the variation in the WF impacts on nighttime LST (figure 6(a)). The path coefficients of the shape index (0.35, $p = 0.09$) and wind speed (0.43, $p < 0.05$) are positive, while the path coefficient of the annual precipitation is negative (−0.54, $p < 0.05$). However, the three factors only explain 9% of the variation in the WF impacts on daytime LST (figure 6(b)). Furthermore, none of the three path coefficients are significant ($p > 0.05$), which also implies that the processes of the WF impacts on daytime LST are more complex than those on nighttime LST.

To further remove the possible influences of different properties of soil types, we also use SEM based on the 12 WFs covered by gypsisols. The results suggest that the three factors can explain 76% of the variation in the WF

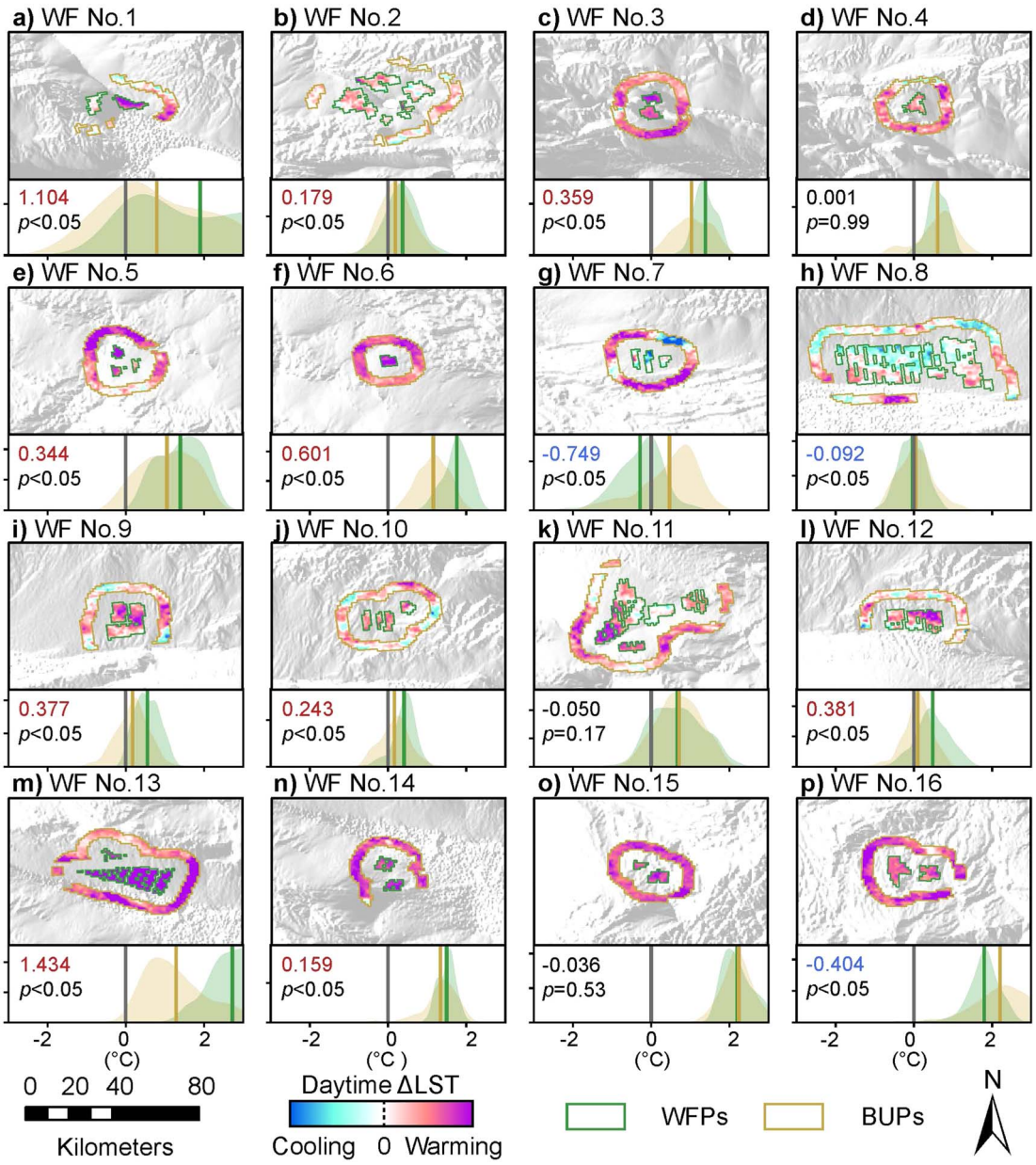

Figure 4. MODIS daytime ΔLST from 2001 to 2018 in 16 WFs. (a)-(p) Spatial distributions of MODIS daytime ΔLST in 18 years periods, respectively. The background images are STRM DEM hill shade images. The kernel density estimation (KDE) plots are the distribution of image values within the WFPs (green) and BUPs (brown). The ΔLST and significance levels of the two-sample t-tests between the image values within the WFPs and BUPs are shown in the KDE plots. Significant warming or cooling ($p < 0.05$) in the WFPs is illustrated by the red or blue color, respectively, of the ΔLST text in the KDE plots.

impacts on nighttime LST (figure 6(c)), and the path coefficient of the shape index is also similar to the SEM established with all the WFs. However, the SEM still could not adequately explain the variations in the WF impacts on daytime LST, although the coefficients of determination increased ($R^2 = 0.16$, figure 6(d)).

In addition, we also apply the SEM in different seasons (figure S13). The results suggest that the three factors can well explain the variations in the WF impacts on night LST in spring ($R^2 = 0.54$), autumn ($R^2 = 0.49$), and winter ($R^2 = 0.54$), but the results suggest a low explanation in summer ($R^2 = 0.13$). The sign of the path coefficients is the same as the results on the annual scale. In contrast, this factor is still unable to well explain the variations in the WF impacts on daytime LST across the different seasons.

4. Discussion

4.1. Processes and magnitudes of wind farm impact on land surface temperature

Previous studies of WF impacts on LST in vegetated regions (grasslands and croplands) indicate that the ΔLST in the nighttime range from −0.18 °C to 0.47 °C, while the ΔLST in the daytime range from −0.26 °C to 0.72 °C

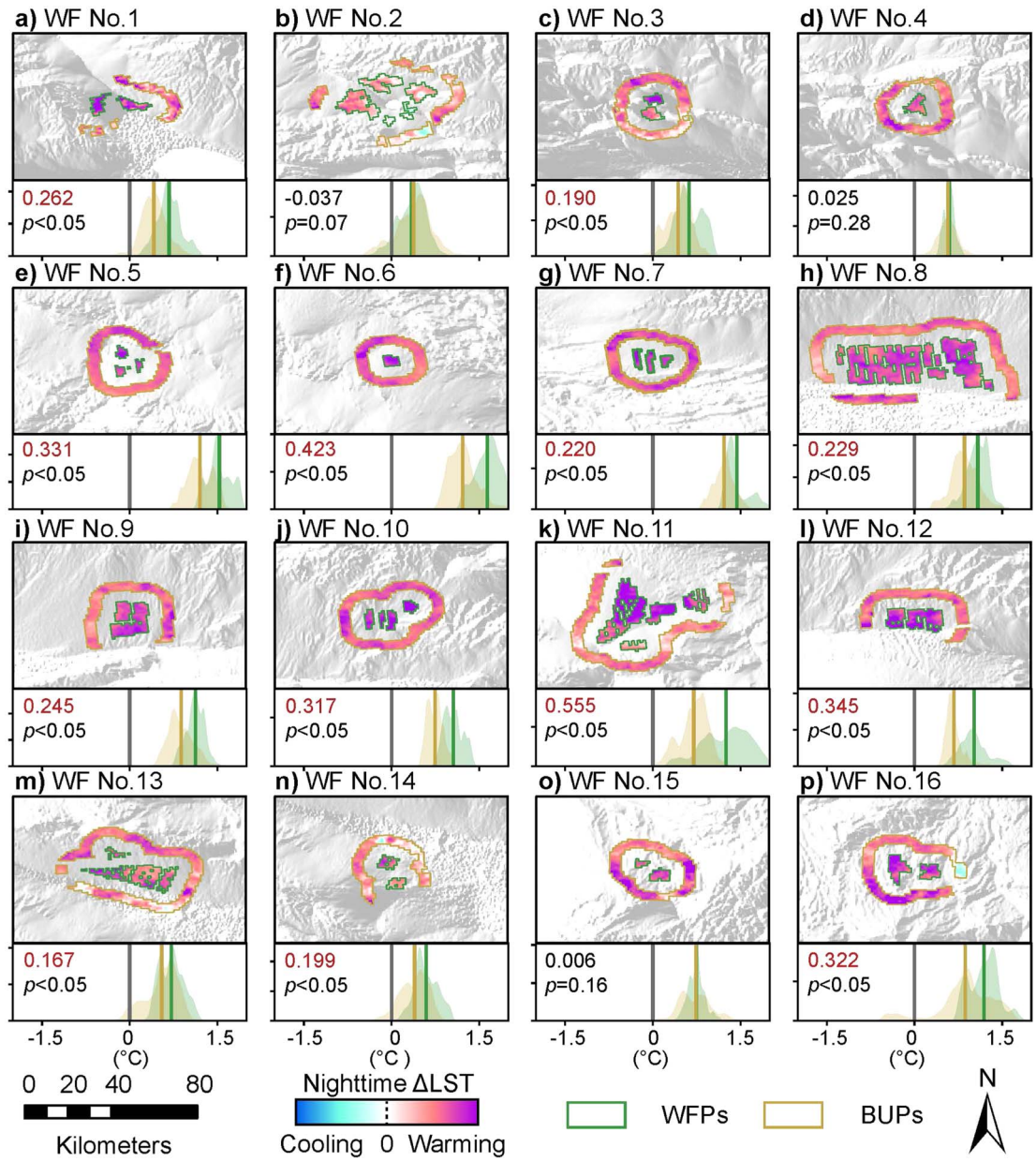

Figure 5. MODIS nighttime ΔLST from 2001 to 2018 at 16 WFs. (a)-(p) Spatial distributions of MODIS nighttime ΔLST of 18 years periods, respectively. The background images are STRM DEM hill shade images. The kernel density estimation (KDE) plots are the distributions of the image values within the WFPs (green) and BUPs (brown). The ΔLST and significance levels of the two-sample t-tests between the image values within the WFPs and BUPs are shown in the KDE plots. Significant warming or cooling ($p < 0.05$) in the WFPs is illustrated by the red or blue color, respectively, of the ΔLST text in the KDE plots.

(Zhou *et al* 2012 2013, Harris *et al* 2014, Slawsky *et al* 2015, Xia *et al* 2016, Tang *et al* 2017, Miller and Keith 2018, Wu *et al* 2019). In comparison, the impacts of desert WFs are more stable (−0.033 °C to 0.543 °C) in the nighttime and more divergent (−0.729 °C to 1.456 °C) in the daytime. This phenomenon may be explained by the interactions between different land cover types and the atmosphere. For example, potential evapotranspiration in croplands and grasslands may increase under the warmer environment caused by WFs. The cooling effects of increased evapotranspiration may ease the WF impacts on daytime LST observed by remote sensing. The higher water contents of leaf and soil in grassland or cropland lead to slower land surface cooling than desert soil (Ceccato *et al* 2001). It should be noted that the previous conclusions of WF impacts on LST are derived from individual WFs with different climatic and environmental backgrounds. Therefore, the background conditions should be considered when comparing the impacts of WFs on different land cover types in the future. The warming impacts are higher in the nighttime in spring, summer, and autumn, but the opposite in winter (figure S5). These might be because of the enhanced likelihood of turbulent induced warming by the increase of ABL stability, which happens more likely in the nighttime. However, in winter, there is a higher probability of inversions by changes in snow cover, and the surface thermal properties are altered by higher

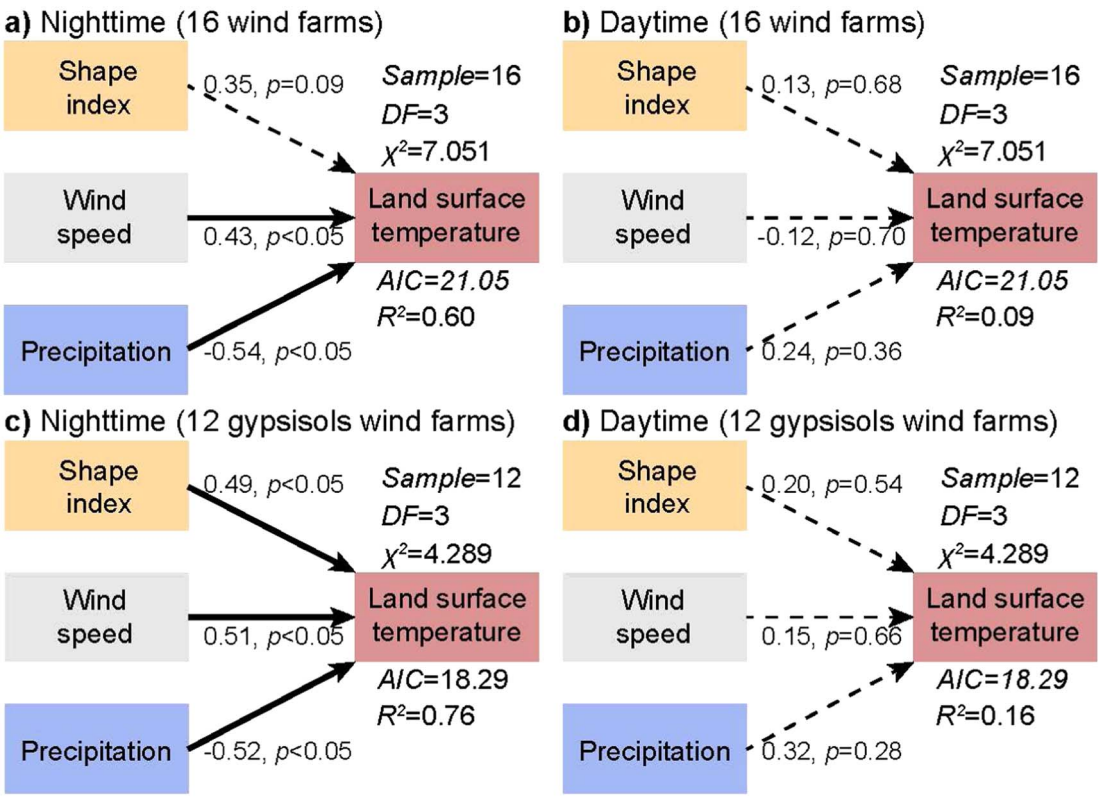

Figure 6. The MODIS daytime and nighttime ΔLST SEM results in 16 WFs and 12 WFs with gypsisols. (a), (b) The SEM relationship between the nighttime and daytime ΔLST and the shape index, MEERA-2 wind speed 50 m above ground, and WorldClim annual precipitation. (c), (d) The SEM relationship between the nighttime and daytime ΔLST and the shape index, wind speed, and precipitation in the 12 WFs with gypsisols. The samples, degree of freedom (DF), Chi-square value (χ^2), Akaike information criterion (AIC), coefficient of determination (R^2) of the SEM, path coefficients, and significances (p) of each factor are given.

albedo and various thermal admittances of snow and ice as well (Oke *et al* 1991). In this study, there is no obvious correlation between nighttime ΔLST and snow cover in winter, the winter ΔLST might be driven by other factors (figure S14).

4.2. Spatial heterogeneity of wind farm impacts on land surface temperature

Based on the optimal structural equation model, annual precipitation, annual mean wind speed, and shape index mainly explain the spatial heterogeneity of the WF impact on nighttime LST. First, the path coefficient of annual precipitation is negative, which means that WFs located in wetter regions with relatively higher evaporation levels may have weaker warming effects. In winter, the thermal properties of snow- and ice-covered surfaces are variable. For instance, the thermal admittance of new snow is low and can support faster warming than desert soil. However, after the snow turns into ice, the thermal admittance becomes higher than that of desert soil, allowing more heat conduction and storage heat and mitigates the observed warming impacts compared to that of the desert soil surface (Oke 2002). In our results, the 4 WFs (Nos. 1, 2, 3, and 4) with higher precipitation (10.38 to 19.91 mm) in winter show weaker warming effects than the remaining 12 WFs (figure S15). Second, the path coefficient of wind speed is positive, which means that WFs located in higher wind speed regions may have stronger warming effects. A higher wind speed can increase the rotation speed of the wind turbine's blades before it meets the rated power (Ragheb and Ragheb 2011); therefore, it may increase the wake turbulence by rotating the blades and then increasing the LST. Third, the path coefficient of the shape index is positive, which means that the WF impacts on LST become more obvious when the WF shape becomes more irregular and fragmentary. Meanwhile, the higher the shape index is, the more dispersed the wind turbines in WF will be, which would help alleviate the wake effects of turbines and mitigate the wind speed loss (De-Prada-Gil *et al* 2015), which might lead to a faster rotation speed. The path coefficients of the other three shape factors are not as high as the shape index because it is the only factor that can indicate the shape complexity within a single WF patch.

However, annual precipitation, annual mean wind speed and shape index cannot well explain the spatial heterogeneity of WF impacts on daytime LST. The Δ surface roughness between the WFPs and BUPs negatively correlates with the ΔLST, which implies that the WFs on surfaces with a lower surface roughness than buffer

regions may cause stronger warming effects. The Δ surface roughness can explain 21% of the variations in all 16 WFs and 31% of the variations in the 12 WFs covered by gypsisols (figures S9(j), S11(j)). The relative surface roughness between WFPs and BUPs might modify the convection of sensible heat between the two regions (Zhao *et al* 2014, Manoli *et al* 2019). When the BUPs are relatively rougher, the heat generated by turbulence effects in the WFPs might be restricted to diffuse into BUPs and could lead to more obvious warming effects. Besides, higher surface roughness in the BUPs may lead to stronger verticle sensible heat flux and suppress surface warming (Potter *et al* 1987), which could make more obvious relative warming in the WFPs. In the nighttime, thermal admittance might affect ΔLST, the lower thermal admittance is in the BUPs, the higher ΔLST is more likely to happen because of low thermal sensitivity match. Moreover, when the Δthermal admittance is higher between WFPs and BUPs, the ΔLST might be higher (Oke *et al* 1991). The relationships between nighttime ΔLST and thermal admittance and Δthermal admittance are weak in our study (figure S16), which might be the result of two sources. The first source is the uncertainties brought by the parameters of thermal admittance calculation, which are given by literatures without experiments. The second source might be the uncertainty of SoilGrids datasets, which are rasterized by soil samples and machine learning algorithms. The sparse desert soil samples in Northwestern China might lead to higher uncertainty than other soil types.

4.3. Uncertainties, implications, and future works

In this work, we use the latest remote sensing products to detect WF impacts on LST, but uncertainties still remain that should be further studied in future research. First, all the wind turbines in each WF were built in the last two decades. However, there are still no datasets on the construction period and operation time for each wind turbine. Because the WF impacts on LST mainly occur when the wind turbines are running, lacking these data obscures the quantification of the WF impacts on LST in our work. Second, wind turbines with higher rated power may generate stronger weak turbulence than turbines with lower rated power (Fan and Zhu 2019). Therefore, providing the rated power for each wind turbine can help us better understand the magnitudes of the WF impacts on LST. Third, there is no obvious averaged difference between MODIS Terra and Aqua ΔLST in the nighttime (0.001 °C), while it is higher in the daytime (0.083 °C) (figure S17). The overpass time of satellite might affect observed ΔLST due to the lower ABL stability in the daytime. Fourth, although long-term remote sensing series are an optimal technological method for studying WF impacts, we still need *in situ* measurements and field experiments to evaluate our results and discover the driving mechanisms.

In previous studies, researchers have simulated WFs with Weather Research and Forecasting (WRF) models (Vautard *et al* 2014, Miller and Keith 2018, Pryor *et al* 2018, Sun *et al* 2018). The current WF module in WRF mainly includes two processes: an elevated sink of momentum and a source of kinetic energy turbulence (Xia *et al* 2019 2017, Zhou *et al* 2020). Although it has been used to simulate WFs in croplands and grasslands, the WRF model does not well consider the complex interactions between vegetation and the atmosphere (Chen *et al* 2016, Gao *et al* 2017). Given that there are marginal interactions between vegetation and the atmosphere in desert WFs, the observation-based results in our study provide a good opportunity for improving the parameterizations in the WRF model.

The terrain within WFs will influence the wind flow and shortwave radiation (Wood 2000), and further affect local ABL stability. However, the coarse spatial resolution of the present MODIS LST datasets is a not good match for analysis of terrain induced micro climate changes. Moreover, the ABL stability in complex terrain in WFs remains uncertain (Kit *et al* 2017). In the future, the impact of terrain could be further discussed with finer resolution datasets based on remote sensing or *in situ* measurement. The sky view factor might influence income shortwave and longwave radiation and further affect ΔLST in WFs (Oke 1981). The sky view factor of WF could be changed by terrain, turbine density, and turbine size, the effect of the sky view factor could be extracted in the future with *in situ* measurements.

The main aim of wind energy is to provide clean electricity and replace fossil fuels to mitigate climate change. However, WFs also increase the local LST based on our results and those of previous studies (Keith *et al* 2004, Zhou *et al* 2012, Li *et al* 2018). Furthermore, large-scale WFs in vegetated regions may also affect ecosystem dynamics (e.g., vegetation growth and soil carbon stability) by changing the local climate (Knapp *et al* 2002, Armstrong *et al* 2014) and affect animal diversity (Marques *et al* 2014, Dai *et al* 2015, Smallwood and Thelander 2008). The WFs reduce greenhouse gas emissions of fossil fuels and mitigate global warming trends while having localized side effects on the environment. Although there might be some disadvantages of desert WFs compared with those in grasslands or croplands, such as high electricity transport costs and potential mechanical damage caused by sand storms (Fiore and Selig 2016, Li *et al* 2018), desert WFs can still yield global energy profits by minimizing environmental costs. Therefore, the potential trade-offs in energy and ecosystems of WFs should be further evaluated in the future to estimate the realistic efficiency of wind energy.

5. Conclusion

Wind farms (WFs) can change the local land surface temperature (LST) through turbulence effects. In this study, we detect the direct impacts on daytime and nighttime LST of 16 desert WFs. Although the averaged impacts of daytime and nighttime LST are comparable, the impacts on nighttime LST are more convergent than those on daytime LST. The spatial heterogeneity of the desert WF impacts on nighttime LST can mainly be explained by environmental factors. However, the divergent impacts of desert WFs on daytime LST cannot be well explained by environmental factors. Our study is the first to provide the spatial patterns of direct WF impacts on LST, which greatly overcomes the potential uncertainties in previous studies induced by interactions between vegetation and the atmosphere. In general, our results provide a benchmark for parameterizing Weather Research and Forecasting (WRF) model processes. Given the rapid development of wind energy, quantifying WF impacts on the local environment besides LST should be considered a high priority in climate change research.

Acknowledgments

This work is supported by National Key R&D Program of China (2022YFF1303401) and the National Natural Science Foundation of China (Grant No.42090012). We thank the editors and anonymous reviewers for improving our work.

Data availability statement

The data that support the findings of this study are openly available at the following URL/DOI: https://doi.org/10.6084/m9.figshare.21202019.v1.

ORCID iDs

Naijing Liu https://orcid.org/0000-0002-6701-3864
Xiang Zhao https://orcid.org/0000-0002-0155-6735
Xin Zhang https://orcid.org/0000-0001-7844-593X
Jiacheng Zhao https://orcid.org/0000-0002-1493-4723
Haoyu Wang https://orcid.org/0000-0003-0785-6592
Donghai Wu https://orcid.org/0000-0002-4638-3743

References

Abo-Khalil A G, Alyami S, Sayed K and Alhejji A 2019 Dynamic modeling of wind turbines based on estimated wind speed under turbulent conditions *Energies* **12** 1907
Armstrong A, Waldron S, Whitaker J and Ostle N J 2014 Wind farm and solar park effects on plant-soil carbon cycling: uncertain impacts of changes in ground-level microclimate *Glob. Change Biol.* **20** 1699–706
Barry-Macaulay D, Bouazza A, Wang B and Singh R 2015 Evaluation of soil thermal conductivity models *Can. Geotech. J.* **52** 1892–900
Ceccato P, Flasse S, Tarantola S, Jacquemoud S and Grégoire J-M 2001 Detecting vegetation leaf water content using reflectance in the optical domain *Remote Sens. Environ.* **77** 22–33
Chen L, Li Y, Chen F, Barr A, Barlage M and Wan B 2016 The incorporation of an organic soil layer in the noah-MP land surface model and its evaluation over a boreal aspen forest *Atmospheric Chem. Phys.* **16** 8375–87
Chinese Wind Energy Association 2019 *China wind power industry mapping* 2018 (Beijing)
Corten G 2000 Heat generation by a wind turbine *14th IEA Symp. on the Aerodynamics of Wind Turbines. pp. 1–8*
Côté J and Konrad J-M 2005 A generalized thermal conductivity model for soils and construction materials *Can. Geotech. J.* **42** 443–58
Dai K, Bergot A, Liang C, Xiang W-N and Huang Z 2015 Environmental issues associated with wind energy—a review *Renew. Energy* **75** 911–21
De-Prada-Gil M, Alías C G, Gomis-Bellmunt O and Sumper A 2015 Maximum wind power plant generation by reducing the wake effect *Energy Convers. Manag.* **101** 73–84
Dorigo W *et al* 2017 ESA CCI soil moisture for improved earth system understanding: state-of-the art and future directions *Remote Sens. Environ.* **203** 185–215
Fan Z and Zhu C 2019 The optimization and the application for the wind turbine power-wind speed curve *Renew. Energy* **140** 52–61
Feng X *et al* 2016 Revegetation in China's Loess Plateau is approaching sustainable water resource limits *Nat. Clim. Change* **6** 1019–22
Fick S E and Hijmans R J 2017 WorldClim 2: new 1-km spatial resolution climate surfaces for global land areas *Int. J. Climatol.* **37** 4302–15
Fiore G and Selig M S 2016 Simulation of damage progression on wind turbine blades subject to particle erosion *54th AIAA Aerospace Sciences Meeting. p. 0813*
Gao Y, Xiao L, Chen D, Chen F, Xu J and Xu Y 2017 Quantification of the relative role of land-surface processes and large-scale forcing in dynamic downscaling over the tibetan plateau *Clim. Dyn.* **48** 1705–21
Gelaro R *et al* 2017 The modern-era retrospective analysis for research and applications, version 2 (MERRA-2) *J. Clim.* **30** 5419–54

Gorelick N, Hancher M, Dixon M, Ilyushchenko S, Thau D and Moore R 2017 Google earth engine: planetary-scale geospatial analysis for everyone *Remote Sens. Environ.* **202** 18–27
Grossiord C, Buckley T N, Cernusak L A, Novick K A, Poulter B, Siegwolf R T, Sperry J S and McDowell N G 2020 Plant responses to rising vapor pressure deficit *New Phytol.* **226** 1550–66
Gruber A, Scanlon T, van der Schalie R, Wagner W and Dorigo W 2019 Evolution of the ESA CCI soil moisture climate data records and their underlying merging methodology *Earth Syst. Sci. Data* **11** 717–39
Harris R A, Zhou L and Xia G 2014 Satellite observations of wind farm impacts on nocturnal land surface temperature in Iowa *Remote Sens.* **6** 12234–46
Hengl T *et al* 2017 Soil grids250 m: global gridded soil information based on machine learning *PLoS One* **12** e0169748
Jarvis A *et al* 2008 Hole-filled SRTM for the globe Version 4, available from the CGIAR-CSI SRTM 90 m database http://srtm.csi.cgiar.org/
Keith D W, DeCarolis J F, Denkenberger D C, Lenschow D H, Malyshev S L, Pacala S and Rasch P J 2004 The influence of large-scale wind power on global climate *Proc. Natl Acad. Sci.* **101** 16115–20
Kit E, Hocut C, Liberzon D and Fernando H 2017 Fine-scale turbulent bursts in stable atmospheric boundary layer in complex terrain *J. Fluid Mech.* **833** 745–72
Knapp A K, Fay P A, Blair J M, Collins S L, Smith M D, Carlisle J D, Harper C W, Danner B T, Lett M S and McCarron J K 2002 Rainfall variability, carbon cycling, and plant species diversity in a mesic grassland *Science* **298** 2202–5
Kummerow C, Barnes W, Kozu T, Shiue J and Simpson J 1998 The tropical rainfall measuring mission (TRMM) sensor package *J. Atmospheric Ocean. Technol.* **15** 809–17
Kurylyk B L, MacQuarrie K T and McKenzie J M 2014 Climate change impacts on groundwater and soil temperatures in cold and temperate regions: Implications, mathematical theory, and emerging simulation tools *Earth-Sci. Rev.* **138** 313–34
Li Y, Kalnay E, Motesharrei S, Rivas J, Kucharski F, Kirk-Davidoff D, Bach E and Zeng N 2018 Climate model shows large-scale wind and solar farms in the Sahara increase rain and vegetation *Science* **361** 1019–22
Manoli G, Fatichi S, Schläpfer M, Yu K, Crowther T W, Meili N, Burlando P, Katul G G and Bou-Zeid E 2019 Magnitude of urban heat islands largely explained by climate and population *Nature* **573** 55–60
Marques A T, Batalha H, Rodrigues S, Costa H, Pereira M J R, Fonseca C, Mascarenhas M and Bernardino J 2014 Understanding bird collisions at wind farms: an updated review on the causes and possible mitigation strategies *Biol. Conserv.* **179** 40–52
McGarigal K 1995 *Fragstats: spatial pattern analysis program for quantifying landscape structure* US Department of Agriculture
Maruyama G 1997 *Basics of Structural Equation Modeling* (New York, NY: Sage)
Meyers R A 2002 *Encyclopedia of Physical Science and Technology* (New York, NY: Academic Press)
Miller L M and Keith D W 2018 Climatic impacts of wind power *Joule* **2** 2618–32
Nematollahi O, Hajabdollahi Z, Hoghooghi H and Kim K C 2019 An evaluation of wind turbine waste heat recovery using organic Rankine cycle *J. Clean. Prod.* **214** 705–16
Oke T, Johnson G, Steyn D and Watson I 1991 Simulation of surface urban heat islands under 'ideal'conditions at night part 2 *Diagnosis of causation. Bound.-Layer Meteorol.* **56** 339–58
Oke T R 1981 Canyon geometry and the nocturnal urban heat island: comparison of scale model and field observations *J. Climatol.* **1** 237–54
Oke T R 2002 *Boundary Layer Climates.* (London: Routledge)
Pahud D 2002 *Geothermal energy and heat storage* Scuola Universitaria Professionale della Svizzera Italiana
Payero J O, Tarkalson D D, Irmak S, Davison D and Petersen J L 2008 Effect of irrigation amounts applied with subsurface drip irrigation on corn evapotranspiration, yield, water use efficiency, and dry matter production in a semiarid climate *Agric. Water Manag.* **95** 895–908
Potter K, Horton R and Cruse R 1987 Soil surface roughness effects on radiation reflectance and soil heat flux *Soil Sci. Soc. Am. J.* **51** 855–60
Pryor S C, Barthelmie R J and Shepherd T J 2018 The influence of real-world wind turbine deployments on local to mesoscale *Climate. J. Geophys. Res. Atmospheres* **123** 5804–26
Qin Y, Li Y, Xu R, Hou C, Armstrong A, Bach E, Wang Y and Fu B 2022 Impacts of 319 wind farms on surface temperature and vegetation in the United States *Environ. Res. Lett.* **17** 024026
Ragheb M and Ragheb A M 2011 Wind turbines theory-the betz equation and optimal rotor tip speed ratio *Fundam. Adv. Top. Wind Power* **1** 19–38
Redmon J, Divvala S, Girshick R and Farhadi A 2016 You only look once: unified, real-time object detection *2016 IEEE Conf. on Computer Vision and Pattern Recognition (CVPR). Presented at the 2016 IEEE Conf. on Computer Vision and Pattern Recognition (CVPR), IEEE, Las Vegas, NV, USA, pp. 779–788*
Roy S B and Traiteur J J 2010 Impacts of wind farms on surface air temperatures *Proc. Natl Acad. Sci.* **107** 17899–904
Runnalls K and Oke T 2000 Dynamics and controls of the near-surface heat island of Vancouver *British Columbia. Phys. Geogr.* **21** 283–304
Slawsky L, Zhou L, Roy S, Xia G, Vuille M and Harris R 2015 Observed thermal impacts of wind farms over northern illinois *Sensors* **15** 14981–5005
Smallwood K S and Thelander C 2008 Bird mortality in the altamont pass wind resource area, California *J. Wildl. Manag.* **72** 215–23
Sun H, Luo Y, Zhao Z and Chang R 2018 The impacts of chinese wind farms on climate *J. Geophys. Res. Atmospheres* **123** 5177–87
Tabassum A, Premalatha M, Abbasi T and Abbasi S A 2014 Wind energy: Increasing deployment, rising environmental concerns *Renew. Sustain. Energy Rev.* **31** 270–88
Tahir A, Elgabaili M, Rajab Z, Buaossa N, Khalil A and Mohamed F 2019 Optimization of small wind turbine blades using improved blade element momentum theory *Wind Eng.* **43** 299–310
Tang B, Wu D, Zhao X, Zhou T, Zhao W and Wei H 2017 The observed impacts of wind farms on local vegetation growth in northern China *Remote Sens.* **9** 332
Torres R, Snoeij P, Geudtner D, Bibby D, Davidson M, Attema E, Potin P, Rommen B, Floury N, Brown M *et al* 2012 GMES sentinel-1 mission *Remote Sens. Environ.* **120** 9–24
Vautard R, Thais F, Tobin I, Bréon F-M, de Lavergne J-G D, Colette A, Yiou P and Ruti P M 2014 Regional climate model simulations indicate limited climatic impacts by operational and planned European wind farms *Nat. Commun.* **5** 3196
Veers P, Dykes K, Lantz E, Barth S, Bottasso C L, Carlson O, Clifton A, Green J, Green P, Holttinen H *et al* 2019 Grand challenges in the science of wind energy *Science* 366
Wan Z, Hook S and Hulley G 2015 Mod11a1 Modis/terra land surface temperature/emissivity daily L3 global 1km SIN grid V006
Wang S and Wang S 2015 Impacts of wind energy on environment: a review *Renew. Sustain. Energy Rev.* **49** 437–43
Wood N 2000 Wind flow over complex terrain: a historical perspective and the prospect for large-eddy modelling *Bound.-Layer Meteorol.* **96** 11–32
World Wind Energy Association 2019 Wind power capacity worldwide reaches 597 GW, 50,1 GW added in 2018 https://wwindea.org/wind-power-capacity-worldwide-reaches-600-gw-539-gw-added-in-2018/

Wu S and Archer C L 2021 Near-ground effects of wind turbines: observations and physical mechanisms *Mon. Weather Rev.* **149** 879–98
Wu X, Zhang L, Zhao C, Gegen T, Zheng C, Shi X, Geng J and Letu H 2019 Satellite-based assessment of local environment change by wind farms in china *Earth Space Sci.* **6** 947–58
Xia G, Cervarich M C, Roy S B, Zhou L, Minder J R, Jimenez P A and Freedman J M 2017 Simulating impacts of real-world wind farms on land surface temperature using the WRF model: validation with observations *Mon. Weather Rev.* **145** 4813–36
Xia G, Zhou L, Freedman J M, Roy S B, Harris R A and Cervarich M C 2016 A case study of effects of atmospheric boundary layer turbulence, wind speed, and stability on wind farm induced temperature changes using observations from a field campaign *Clim. Dyn.* **46** 2179–96
Xia G, Zhou L, Minder J R, Fovell R G and Jimenez P A 2019 Simulating impacts of real-world wind farms on land surface temperature using the WRF model: physical mechanisms *Clim. Dyn.* **53** 1723–39
Zhang X, Han L, Han L and Zhu L 2020 How well do deep learning-based methods for land cover classification and object detection perform on high resolution remote sensing imagery? *Remote Sens.* **12** 417
Zhao L, Lee X, Smith R B and Oleson K 2014 Strong contributions of local background climate to urban heat islands *Nature* **511** 216–9
Zhou L, Baidya Roy S and Xia G 2020 Weather, climatic and ecological impacts of onshore wind farms *Reference Module in Earth Systems and Environmental Sciences.* (Netherlands: Elsevier)
Zhou L, Tian Y, Baidya Roy S, Thorncroft C, Bosart L F and Hu Y 2012 Impacts of wind farms on land surface temperature *Nat. Clim. Change* **2** 539–43
Zhou L, Tian Y, Chen H, Dai Y and Harris R A 2013 Effects of topography on assessing wind farm impacts using MODIS data *Earth Interact.* **17** 1–18